Oriented naphthalene-O-propylammonium based $(NOP)_4AuB^{III}I_8$ Ruddlesden-Popper Two-Dimensional Gold Double Perovskite Thin Films Featuring High Charge-Carrier Mobility

Florian Wolf [a], Thanh Chau [a], Dan Han [b,c], Kieran B. Spooner [c], Marcello Righetto [d], Patrick Dörflinger [e], Shizhe Wang [a], Roman Guntermann [a], Rik Hooijer [a], David O. Scanlon [c], Hubert Ebert [a], Vladimir Dyakonov [e], Laura M. Herz [d,f], and Thomas Bein [a*]

[a] Department of Chemistry and Center for NanoScience (CeNS), University of Munich (LMU), Butenandtstraße 5-13, 81377 Munich, Germany

[b] School of Materials Science and Engineering, Jilin University, Changchun, 130012, China

[c] School of Chemistry, University of Birmingham Edgbaston, Birmingham B15 2TT, United Kingdom

[d] Department of Physics, University of Oxford, Clarendon Laboratory, Parks Road, Oxford, OX1 3PU, United Kingdom

[e] Experimental Physics VI, University of Würzburg, Am Hubland, D-97074 Würzburg

[f] Institute for Advanced Study, Technical University of Munich, Lichtenbergstrasse 2a, D-85748 Garching, Germany

KEYWORDS :2D double perovskite, photodetector, conductivity, gold, bismuth, antimony, aromatic spacer cation.

ABSTRACT: Two-dimensional perovskites show intriguing optoelectronic properties due to their anisotropic structure and multiple quantum well structure. Here we report the first three gold based Ruddlesden-Popper type two-dimensional double perovskites with a general formula $(NOP)_4Au^IB^{III}I_8$ employing naphthalene-O-propylammonium (NOP) as organic cation. They were found to form highly crystalline thin films on various substrates, predominantly oriented in [001] direction with large domain sizes in the range of ~µm. The thin films show strong optical absorption in the visible, with band gap energies between 1.48 eV and 2.32 eV. Density functional theory calculations support the experimentally obtained band gap energies and predict high charge-carrier mobilities and effective charge separation. A comprehensive study with time-resolved microwave conductivity (TRMC) and optical pump- THz-probe (OPTP) spectroscopy revealed high charge-carrier mobilities for lead-free two-dimensional perovskites of $4.0 \pm 0.2\ cm^2(V\ s)^{-1}$ and charge-carrier lifetimes in the range of µs. Photoconductivity measurements under 1 sun illumination demonstrated the material's application as a photodetector, showing a twofold increase in conductivity when exposed to light.

Introduction:

In recent years, organic-inorganic perovskite-based materials with the molecular formula ABX_3, with methylammonium (MA) lead iodide $MAPbI_3$ as its most prominent representative, have attracted significant attention in material sciences due to their outstanding performance as light absorbing materials, their remarkable optoelectronic properties, efficient synthesis, and potential for future photovoltaic technology to address the global climate crisis.[1] However, lead-based perovskite materials suffer from toxicity issues and often lack sufficient long-term stability under illumination or exposure to moisture and air.[2]

To address these issues, lead-free alternatives have raised considerable interest, including double perovskites with the general formula of $(A^+)_2B^IB^{*III}X_6$ containing one monovalent and one trivalent B-site cation.[3,4] Due to the wide range of possibilities regarding the A- and B-site cations within the Goldschmidt tolerance factor limits, a large variety of double perovskites are accessible, with $Cs_2AgBiBr_6$ as the most prominent example.[3–5] However, the presence of two different B-site elements in double perovskites often limits desirable optoelectronic properties, such as a direct band gap, low band gap energy, and long charge-carrier lifetimes.[3,6] Hence, introducing elements with both mono-valent and trivalent oxidation states accessible, such as Au, offers a potential solution.[5,7] Accordingly, fully inorganic mixed-valence gold halide compounds $Cs_2[Au^{I}X_2][Au^{III}X_4]$ (X = Cl, Br, I) with a distorted 3-dimensional perovskite structure were investigated as potential superconductors in the past[8–11], and show strong charge-transfer interactions arising from their strong electron-phonon coupling caused by the Jahn-Teller effect. Such materials regained scientific interest after calculations and experiments suggested a direct bandgap of 1.1 – 1.3 eV for the Cs_2AuAuI_6 double perovskite, highlighting their potential as light absorbing material.[7,12,13] However, film formation of this particular 3D perovskite material remains a challenge, and so far, all studies have been conducted either on powders or single crystals.[5]

In this context, we posit that combining the promising optoelectronic properties of Cs_2AuAuI_6 with the vast design space and typical superior film-forming behavior of 2-dimensional (2D) perovskites containing organic cations could be a promising strategy to overcome the limitations of the 3D bulk material. 2D perovskite-related organic-inorganic hybrid materials have emerged as intriguing novel types of semiconductors, offering both high stability and remarkable chemical and structural tunability.[14] One class, namely Ruddlesden-Popper (RP) 2D double perovskites with $n = 1$ octahedral layers and the general formula $(OC^+)_4B^IB^{III}X_8$ is characterized by alternating single layers of organic cations (OC) and inorganic corner-sharing octahedra. These compounds exhibit high chemical and environmental stabilities and superior film formation qualities, but also possess anisotropic electronic properties arising from their layered structure, yielding generally lower electrical conductivity in the out-of-plane direction. The large organic cation usually has a smaller dielectric constant and different electronic properties than the inorganic octahedral layer, resulting in periodically alternating quantum wells.[15]

Addressing the out-of-plane conductivity limitation, monovalent p-stacking aromatic organic cations with extended p-systems and strong intramolecular hydrogen bonds such as naphthalene or pyrene-based cations were found to enhance out-of-plane charge-carrier transport in RP phases.[16] Implementing these cations in Pb and lead-free Ag, Cu and Bi containing perovskites results in RP 2D double perovskite thin films with outstanding out-of-plane conductivity for 2D perovskites.[14,16] To the best of our knowledge, no gold-based RP-type 2D perovskites with cations larger than MA have been reported.[17] So far, only limited research has been conducted on gold-based organic-inorganic 2D materials. In 2003, Dion-Jacobson (DJ) type related 2D gold perovskites $[NH_3(CH_2)_nNH_3]_2[(Au^{I}I_2)(Au^{III}I_4)(I_3)_2]$ (n =7 and 8) were synthesized.[18] Since then, other mixed-valence organic inorganic hybrid gold iodide polymorphs with organic cations such as methylammonium in $(MA)_2(Au^{I}I_2)(Au^{III}I_4)$ [19] and with other small organic cations like formamidinium (FA), guanidinium (GUA), imidazolium (IMD) or piperidinium (PIP) have been reported.[20] However, these compounds still exhibit distorted 3D perovskite structures or 0-dimensional character and cannot be considered layered structures. A study investigating chain-length dependent changes in crystal structure of $[NH_3(CH_2)_nNH_3]_2[(Au^{I}I_2)(Au^{III}I_4)(I_3)_2]$ revealed the formation of DJ type materials only for OC with chain length n = 7 and n = 8, while lower and higher n-values led to the formation of zero-dimensional structures.[17] Based on the above findings, we posit that integrating organic cations with larger π-systems and significant electronic coupling into gold-containing 2D perovskites could make gold-based RP 2D double perovskites accessible, while simultaneously resulting in enhanced charge transfer properties.

Here, we present three novel $(NOP)_4Au^{I}B^{III}I_8$ (B = Au, Bi, Sb) gold-based Ruddlesden-Popper 2D perovskites incorporating naphthalene-O-propylammonium (NOP^+) as the large organic cation, cast as highly crystalline thin films *via* spin coating from a precursor solution. Our thorough investigation of these new materials includes details of the crystal structure and thin film orientation, which demonstrate a strong orientation of the films parallel to the substrate surface. Furthermore, we report strong optical absorption features in the visible region, indicating a direct band gap character. Moreover, these materials exhibit high charge-carrier mobilities and photo conductivities, which were established by means of terahertz and microwave conductivity measurements, making them promising candidates for optoelectronic application. Lastly, the significant response as a photodetector for visible light obtained fully demonstrates the great potential of these materials

Structural characterization:

The three-dimensional perovskite structure with the general formula ABX_3 comprises corner-sharing BX_6 octahedra with a divalent cation B^{2+} and the halide anion X^-. Within this structure, the cuboctahedral cavities are occupied by monovalent cations A^+. Substituting the monovalent A^+ cation with a larger organic cation (OC) disrupts the three-dimensional perovskite framework due to the inability of the oversized OC to fit within the cuboctahedral cavities. The substitution of A^+ with stochiometric amounts of monovalent OCs results in so-called Ruddlesden Popper (RP) 2D perovskites with an octahedral layer thickness of $n = 1$ that adhere to the general formula $(OC)_4B^IB^{III}X_8$. In these structures, the organic cations segregate the inorganic octahedral layers, positioning their positively charged terminal groups, e.g. $-NH_3^+$, into the half-cuboctahedral cavities. The uncharged segments of the organic cations interact via van der Waals (v.d.W) forces or dipole-dipole interactions, thereby establishing a v.d.W gap between the organic layers. As noted above, using the naphthalene-O-propylammonium cation (NOP^+) with its extended conjugated π-system as OC is anticipated to enable the formation of RP 2D double perovskites with significant out-of-plane conductivity.[14,16]

The crystal structures of all three compounds were obtained through Rietveld refinement of powder XRD data of material removed from thin film samples. Investigating the structural properties of the three 2D gold perovskites NOP- AuAu ($(NOP)_4AuAuI_8$), NOP-AuBi ($(NOP)_4AuBiI_8$), and NOP-AuSb ($(NOP)_4AuSbI_8$) we start with a model based on NOP-AgBi adapted from Hooijer *et. al.*[14] and find distorted inorganic $Au^{I}B^{III}I_8$ octahedral layers that are separated by NOP^+ cations as shown in **Figure 1a.** $Au^{I}I_6$- and $B^{III}I_6$-octahedra are corner-connected, forming an inorganic $Au^{I}B^{III}I_8$-layer with a checkerboard pattern ordering of Au^{I} and B^{III}.

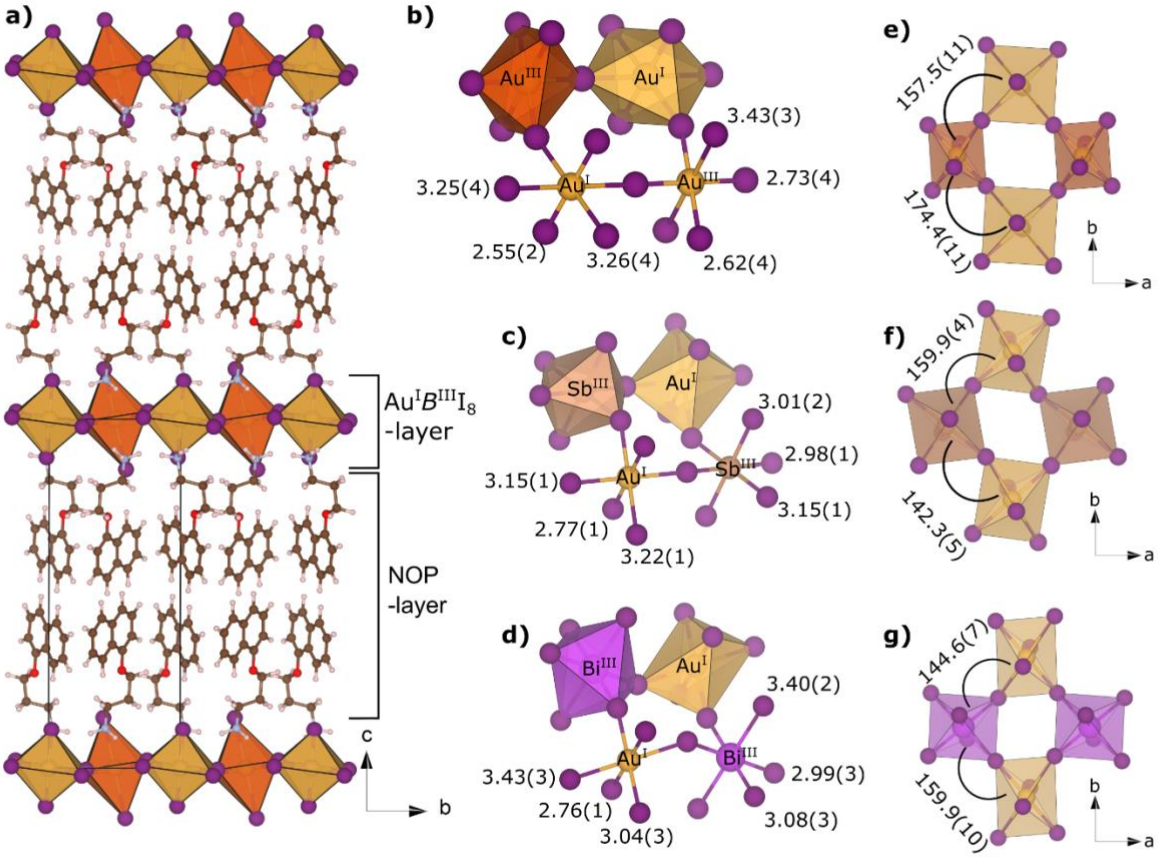

Figure 1. **a)** Crystal structures of $(NOP)_4Au^{I}B^{III}I_8$, **b), c), d)** local coordination of corner-shared $Au^{I}I_6$- and $B^{III}I_6$-octahedra in $Au^{I}B^{III}I_8$-layer, bond lengths are given in Å, **e), f), g)** Au^{I}-I-B^{III} angles in degrees, showcasing the distortion of the inorganic octahedral layer.

The NOP-AuAu compound features two different distorted AuI_6 octahedra due to the mixed valence of gold in Au^{I} and Au^{III}. The linear $[Au^{I}I_2]^-$ anions with bond lengths of Au^{I}-I =2.55 Å are surrounded by square planar $[Au^{III}I_4]^-$ anions with Au^{III}-I = 2.62-2.73 Å. Considering the additional neighboring I atoms for $[Au^{I}I_2]^-$ and $[Au^{III}I_4]^-$ anions, a distorted $Au^{I}Au^{III}I_8$-octahedral layer is formed as seen in **Figure 1b**. Similar bond lengths and distances have been observed in the series of mixed valence AAuI$_3$ compounds (A = K, Rb, Cs), which also feature linear $Au^{I}I_2^-$-(Au^{I}-I = 2.56-2.57 Å) and square planar $Au^{III}I_4^-$-anions (Au^{III}-I = 2.64-2.65 Å).[21–23] For NOP-AuSb and NOP-AuBi, a similar coordination of the $[Au^{III}I_4]^-$ anions is found but with slightly elongated Au^{I}-I bonds (Au^{I}-I = 2.76-77 Å) along the linear $Au^{I}I_2$ unit (**Figure 1 c-d**). Sb^{III} and Bi^{III} in comparison are coordinated octahedrally with only a minor tetragonal distortion represented by 4 short bond lengths (Sb-I = 2.98-3.01 Å, Bi-I = 2.99-3.07 Å) and 2 slightly elongated bonds (Sb-I = 3.15 Å, Bi-I = 3.40 Å) observed. Comparing the three octahedral layers as shown in Figure 1 e-g, different degrees of distortions and tilting are apparent. Between $Au^{I}I_6$, $Au^{III}I_6$, $Sb^{III}I_6$ and $Bi^{III}I_6$, different octahedral sizes and shapes are present, which result in different void-sizes and -shapes available for the organic spacer cations, making a comparison of the interactions between the inorganic layers and the OC difficult. Nevertheless, when comparing the different B(III) ion sizes according to Shannon[24] (Sb^{III}: 0.76 Å; Au^{III}: 0.85 Å; Bi^{III}: 1.03 Å), one would expect a B(III)I_6 octahedral volume increase (Table S2). The N-I distances are very similar to those in NOP-Pb.[16] Due to the high distortion of the octahedral layer, we hereby only compare the shortest N-I distances to give a rough estimate of the interactions between the OC and the inorganic layers. They are as follows: NOP-AuAu = 3.53 Å, NOP-AuBi = 3.32 Å and NOP-AuSb = 3.21 Å, which shows the same trend as the experimentally obtained band gap values from Tauc plots (E_g(NOP-AuAu) = 1.48 eV; E_g(NOP-AuBi) = 2.20 eV; E_g(NOP-AuSb) = 2.32 eV).

The Ruddlesden-Popper 2D perovskite structure type with the octahedral layer thickness of $n = 1$ was confirmed for all three novel materials by Rietveld-refinement of powder XRD data, utilizing an existing Ruddlesden-Popper 2D perovskite single crystal structure dataset of $(NOP)_4AgBiI_8$ as a starting model.[14] A full set of crystal data is given in the supporting information.

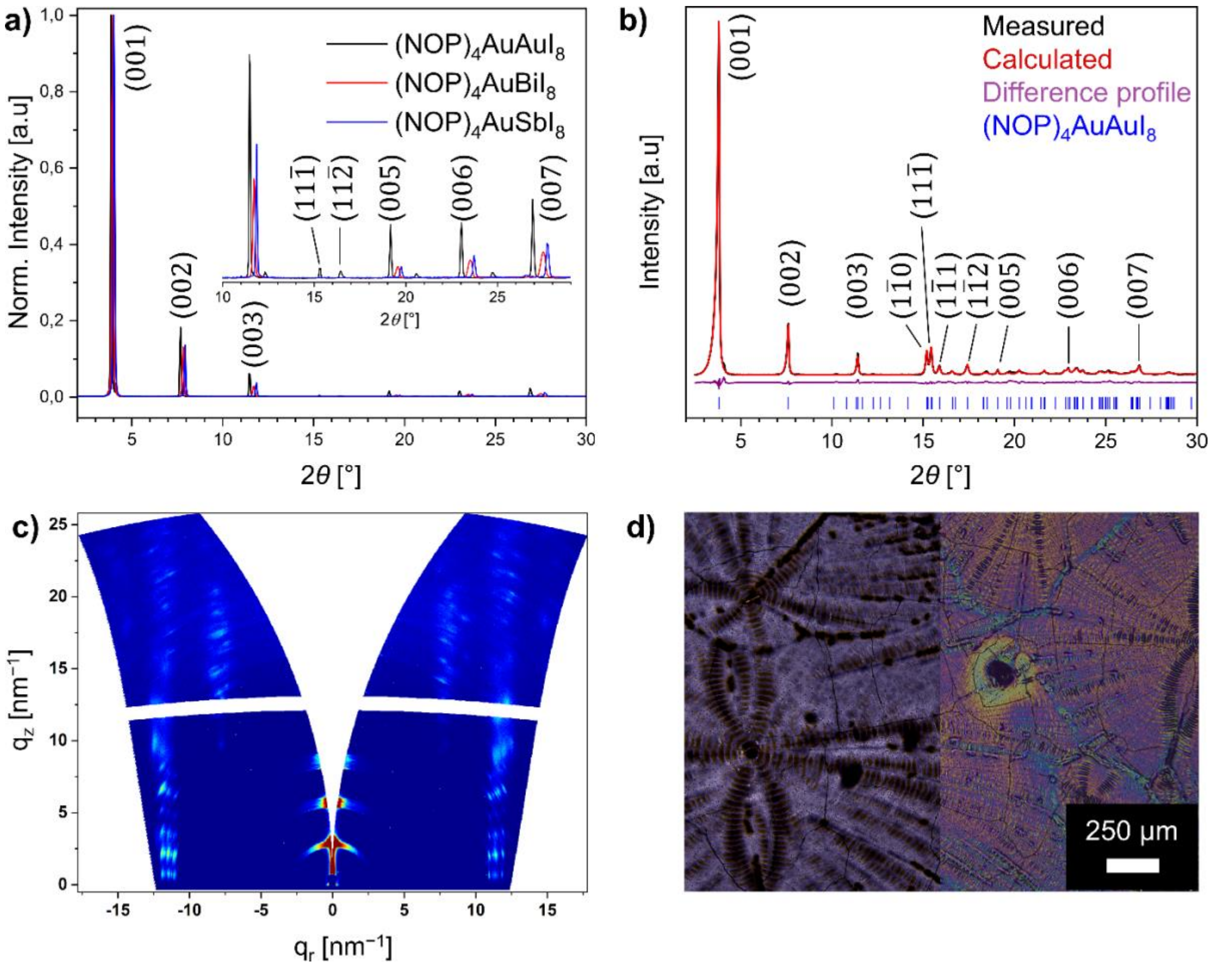

Figure 2. **a)** Normalized XRD patterns of thin film samples of NOP-AuAu, NOP-AuBi, and NOP-AuSb. **b)** Powder XRD used for Rietveld-refinement of scratched-off and ground NOP-AuAu material. **c)** GIWAXS image of NOP-AuAu on a 7 Ω/cm² FTO substrate, measured with an incident angle of $\alpha_i = 0.2°$. **d)** Optical microscopy images of NOP-AuAu thin film on an FTO substrate in transmission and direct illumination.

Thin film morphology & orientation:

Following the analysis of the 2D perovskite crystal structure, we now focus on the 2D perovskite thin film morphology. The structures and high crystallinity of the thin films were confirmed through X-ray diffraction (XRD) analysis in Bragg-Brentano geometry. The crystal lattice parameters vary with the N-I distances between the organic cation´s N-atom and inorganic layer´s I-atoms, evidenced by a shift to smaller diffraction angles (2θ) as the distance increases from NOP-AuSb to NOP-AuBi to NOP-AuAu, as shown in **Figure 2a**. Unlike the powder XRD utilized for Rietveld refinement **Figure 2b**, thin film XRD exhibits a limited number of reflections, indicating a preferential crystal growth direction. The observed dominant reflections correspond to the {001} crystallographic planes orthogonal to the c-axis, referred to as the "out-of-plane" direction in 2D perovskites.

The crystalline orientation of the thin films was further evaluated using Grazing Incidence Wide Angle X-ray Scattering (GIWAXS) measurements. The data reveal a strong preferential orientation, with both organic and inorganic layers aligned parallel to the substrate surface, as initially indicated by the thin film XRD data. This is evidenced for NOP-AuAu by the reflections originating from the {00ℓ} planes, which are situated centrally at qr = 0 nm⁻¹ along the azimuthal angle χ = 0° (**Figure 2c**).

Additional reflections observed here correspond to the (10ℓ) and (01ℓ) planes at qr ≈ 8 nm^{-1}, and the (11ℓ) planes at qr ≈ 12 nm^{-1}. On FTO substrates, the preferred orientation of the materials in the out-of-plane direction is more prominent for NOP-AuAu and NOP-AuSb than for NOP-AuBi, the latter showing a more random crystal orientation as demonstrated by more pronounced semicircle reflections in the GIWAXS pattern. The differences in surface roughness and physical properties between Al_2O_3-nanoparticle covered glass and FTO substrates impact film orientation. Hence, NOP-AuAu and NOP-AuSb films fabricated on Al_2O_3-nanoparticle covered glass substrates exhibit a marginally reduced preferential orientation, while still preserving the overall orientation seen in films on FTO substrates. In contrast, for NOP-AuBi an opposite trend is observed, with a higher degree of crystal orientation on the Al_2O_3-nanoparticle covered glass substrate (**Figure S6**). To exclude structural changes depending on the substrates, a detailed study of the influence of the substrate on crystal lattice constants was conducted, utilizing thin-film XRD for NOP-AuAu films on two different FTO-coated glass substrates with different resistances (15 Ω cm^{-2} and 7 Ω cm^{-2}), ITO-coated glass and pristine glass substrates, revealing no significant influence of the substrate's nature on either the crystallinity or the crystal lattice constants (**Figure S5**).

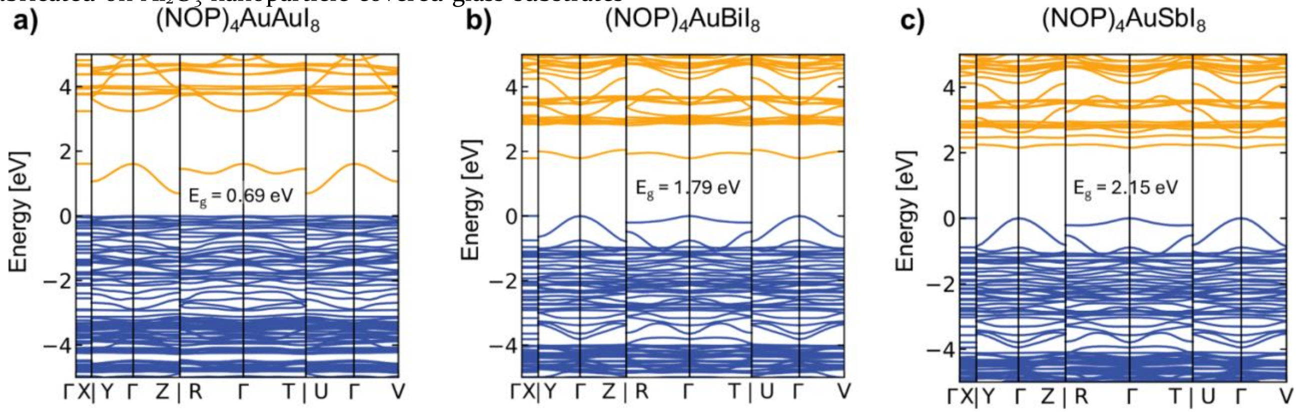

Figure 3. Electronic band structure calculated with HSE06-SOC with valence bands in blue and conduction bands in yellow, for $(NOP)_4AuAuI_8$ (**a**), $(NOP)_4AuBiI_8$ (**b**) and $(NOP)_4AuSbI_8$ (**c**).

Thin film morphology of the three 2D RP double perovskites on FTO substrates was further evaluated with optical microscopy and scanning electron microscopy. All three materials form homogeneous crystalline films with good substrate coverage, large domain and crystallite sizes and a small number of pinholes, as shown for NOP-AuAu in **Figure 2d**. These findings are in good agreement with previously reported crystallization behavior of anisotropic 2D RP materials. Due to their homogeneity, high crystallinity, and similar preferred crystal orientation parallel to the substrate normal along the [001] direction, they are suitable materials for the investigation of optoelectronic properties originating from changing the B^{III+} cation.

Electronic Structures and Band Alignment:

The calculated fundamental band gaps at the HSE06+SOC level of $(NOP)_4AuAuI_8$, $(NOP)_4AuBiI_8$, and $(NOP)_4AuSbI_8$ are 0.69 eV, 1.79 eV and 2.15 eV, respectively. As shown in **Figure 3a, b, c**, NOP-AuAu is an indirect band gap semiconductor with VBM and CBM located at the Γ and Z points, while NOP-AuBi and NOP-AuSb exhibit direct band gaps at the Γ point. The fundamental band gap of NOP-AuAu is much smaller than the measured optical band gap of 1.48 eV obtained with a Tauc plot. The differences between the calculated fundamental band gaps and the experimentally measured ones are acceptable for NOP-AuBi and NOP-AuSb. Moreover, the calculated band gap decreases from NOP-AuSb to NOP-AuBi to NOP-AuAu, which is similar to that of the experimentally measured band gaps.

To understand the origin of this behavior, the density of states and the dipole transition matrix were analyzed. As shown in **Figure S7,** both the inorganic part (Au-5d orbitals and I-5p orbitals) and the organic cations (C-2p orbitals and O-2p orbitals) contribute to the valence band maximum (VBM), showing the mixed states around the VBM. However, the conduction band minimum (CBM) is predominantly composed of the inorganic component (Au-5d orbitals and I-5p orbitals) of $(NOP)_4AuAuI_8$. For $(NOP)_4AuBiI_8$ and $(NOP)_4AuSbI_8$, as shown in **Figure S7** their VBMs are composed of Au-5d and I-5p orbitals, and their CBMs comprise dominant contributions of the Bi/Sb-6p orbitals and I-5p orbitals, which ultimately forms a type I band alignment for the 2D hybrid organic and inorganic perovskite quantum well structure.[14,25,26]

In addition, **Figure S8** displays the sum of the squares of transition dipole moment (TDM) matrix elements of NOP-AuAu, NOP-AuBi, and NOP-AuSb. The TDM matrix elements are zero for the Z point and the Γ point of NOP-AuAu, denoting that the transition probabilities between the highest occupied states and lowest unoccupied states at the Z or Γ point are zero. On the contrary, the TDM matrix elements of NOP-AuBi and NOP-AuSb at the Γ point are large. Thus, the observation of NOP-AuAu showing the smallest band gap can be attributed to its indirect band gap and to a dipole-forbidden transition. In addition, the spin-orbit coupling has a much stronger effect on NOP-AuBi than on NOP-AuSb, as there is a larger p-orbital splitting of the CBM in the former, which leads to the bigger reduction of the band gap of NOP-AuBi compared to NOP-AuSb.

The effective masses of holes and electrons along different directions were evaluated based on the parabolic band dispersion, which is summarized in **Table S4**. The small band dispersion would result in theoretically infinite charge-carrier effective mass, thus the effective mass along these directions were not calculated. Notably, the out-of-plane electron effective mass of NOP-AuAu is much smaller than those of NOP-AuBi and NOP-AuSb. However, NOP-AuAu exhibits a much larger hole effective mass than NOP-AuBi and NOP-AuSb. The difference between the hole and electron effective masses and therefore their mobilities in combination with the unique mixed states around the VBM of NOP-AuAu would enhance its charge-carrier separation.

In addition to the effective masses, we calculated drift mobilities *via* the momentum relaxation time approximation (MRTA) to the Boltzmann transport equation (BTE), (**Table S4**), where we find the highest values for NOP-AuAu and the lowest values for NOP-AuSb, confirming the trend of the experimentally obtained mobility values, which will be discussed below.

Optical properties:

To determine the experimental optical band gap energies of the thin film samples, we employed UV/Vis-spectroscopy on the thin film samples in reflectance as well as in transmittance to calculate absorbance. As theoretical calculations revealed the direct nature of the band gap for $(NOP)_4AuBiI_8$ and $(NOP)_4AuSbI_8$, the Tauc plots for the direct allowed transitions are shown in **Figure 4b**. The absorption spectra show a blue-shift of the absorption onset from NOP-AuAu over NOP-AuBi to NOP-AuSb. The corresponding experimental band gap energies are 1.48 eV, 2.20 eV and 2.32 eV for NOP-AuAu, NOP-AuBi and NOP-AuSb, respectively. NOP-AuAu clearly exhibits a narrower bandgap, and its main absorption peak is blue-shifted when replacing the Au(III) cation with Bi(III) and Sb(III). We attribute this effect to the replacement of Au(6p) with Bi(5p) and Sb(4p) contributions to the conduction band.

For the latter two materials NOP-AuBi and NOP-AuSb, the experimental band gap energies align well with theoretical calculations, confirming the trend of increasing band gap energy from NOP-AuAu to NOP-AuSb. However, for NOP-AuAu the theoretical calculations predict a fundamental indirect bandgap with an energy of 0.69 eV, while experimental data indicate a direct transition at 1.48 eV. This discrepancy between theory and experiment can be attributed to the weak dipole transition between the valence band maximum (VBM) and conduction band minimum (CBM), as described above. Since the transition dipole moment TDM is zero at both the VBM and CBM (see SI) this, with $e \propto (TDM)^2$, results in an absorption coefficient equal to zero for the forbidden dipole transition between the VBM and CBM. Hence, this effect makes the allowed dipole transition with the lowest energy at 1.48 eV the first observable absorption.

In the absorption spectra, for NOP-AuAu and NOP-AuBi a prominent isolated absorption feature centered at 715 nm (1.73 eV; NOP-AuAu) and 504 nm (2.44 eV; NOP-AuBi) is visible and for NOP-AuAu an additional second prominent absorption maximum at 533 nm (2.33 eV) is also present. Similar absorption maxima are frequently observed in the absorption spectra of 2D lead-perovskites as well as for lead-free 2D double perovskites (2D DPs) like $(BA)_4AgBiBr_8$ or the related lead-free 3D double perovskite $Cs_2AgBiBr_6$.[15,27] Furthermore, the related gold-based 3D perovskite Cs_2AuAuI_6 also showed a similar feature in theoretical calculations and experimentally determined absorption spectra, which Kojima *et al.* assigned to the inter-valence charge-transfer transition between Au^I and Au^{III}.[7,12,28] Notably, $(NOP)_4AuSbI_8$ does not show such a prominent distinguishable absorption maximum and only exhibits a weak absorption shoulder at around 482 nm (2.57 eV), which we explain with reduced spin-orbit coupling of Sb(4p) compared with Au(6p) and Bi(5p). The above well-defined absorption peaks could be attributed to excitonic excitations, analogous to those observed in two-dimensional lead perovskites, given that both systems exhibit quantum confinement with Wannier-type excitons being restricted to the inorganic octahedral framework.[15,29] However, this assumption is challenged by the

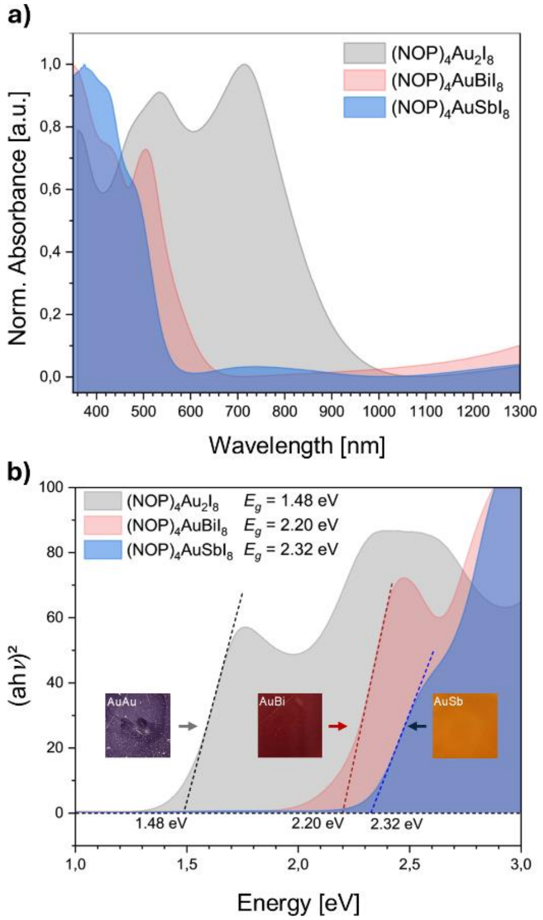

Figure 4: **a)** Normalized UV/Vis absorption spectra and **b)** Tauc plots for a direct allowed transition for (NOP)$_4$AuB^{III+}I$_8$ thin films on FTO substrates, with color coding for different samples given in the graphs. Insets in **b)** show images of the corresponding thin film samples.

fact that theoretical absorption spectra at HSE06+SOC level for similar 2D DPs conducted by Jana *et al.*, neglecting excitonic effect, still exhibit the characteristic maxima, which they assigned to charge transfer transitions between Ag and Bi.[30] Furthermore, no photoluminescence could be experimentally detected, neither at room temperature for all three materials nor at low temperatures for NOP-AuAu, which was selected as an example due to the most prominent absorption maximum. Photoluminescence, however, would usually be expected for a purely excitonic origin of these absorption maxima.[14,15,31] A comprehensive understanding of the optical absorption processes in lead-free 2D DPs remains less developed compared to other well-studied semiconductors, due to the simultaneous presence of multiple effects and carrier species, and a detailed analysis is beyond the scope of this work.[15] However, we emphasize that all three materials show high optical absorption in the visible spectral range and that the band gap energy of NOP-AuAu is in the favorable energy range for single-junction solar cells.

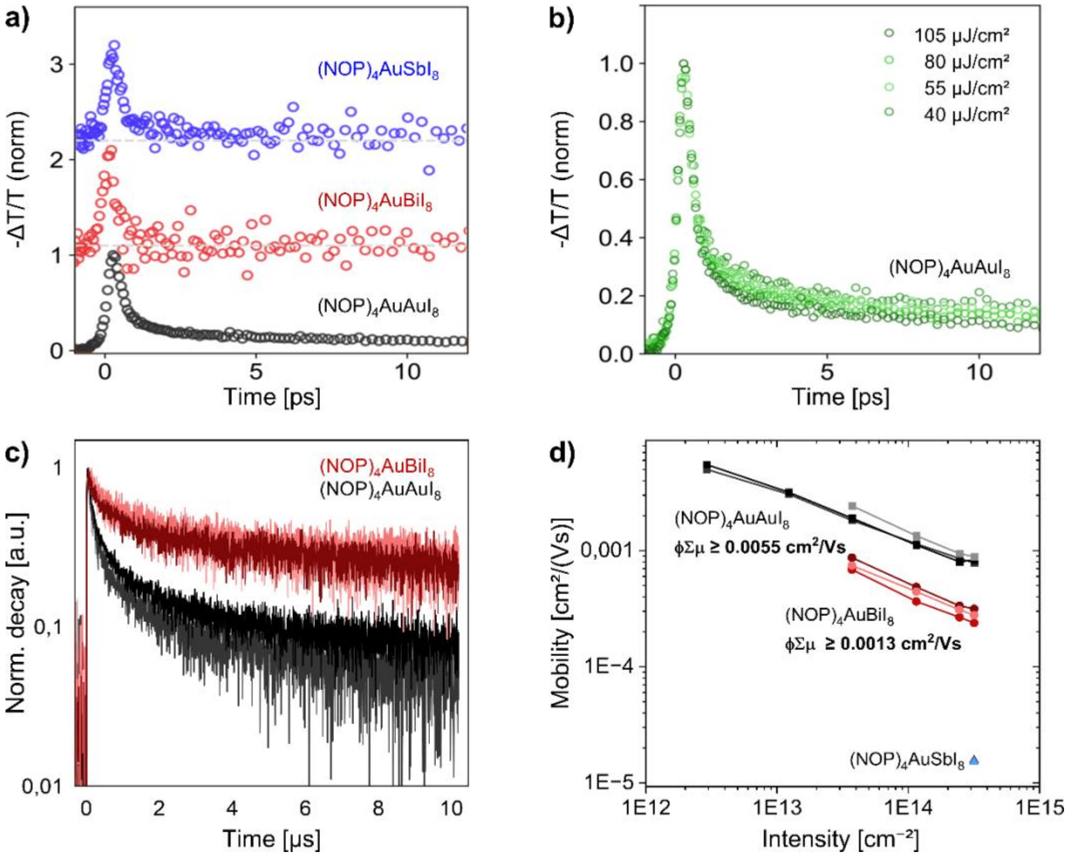

Figure 5. THz photoconductivity transients for Au-based 2D perovskites. **a)** Normalized comparison between optical pump terahertz probe (OPTP) transients for (NOP)$_4$AuSbI$_8$ (light blue), (NOP)$_4$AuBiI$_8$ (red), and (NOP)$_4$AuAuI$_8$ (black). OPTP transients were measured following 3.1-eV photoexcitation with 150 µJ/cm^2 for (NOP)$_4$AuSbI$_8$ and (NOP)$_4$AuBiI$_8$, and 105 µJ/cm^2 for (NOP)$_4$AuAuI$_8$. Data were shifted vertically for visualisation purposes, dashed grey lines represent the reference zero value for the shifted curves. **b)** Normalized comparison between fluence-dependent OPTP transients measured for (NOP)$_4$AuAuI$_8$ following 3.1-eV photoexcitation. **c)** Charge-carrier lifetime decays from TRMC measurements of NOP-AuAu and NOP-AuBi. Mobilities and charge carrier lifetimes of NOP-AuSb could not be determined, due to low signal. Increasing excitation power leads to higher charge carrier density and therefore to faster recombination, partly exceeding the response time of the setup, resulting in a decreased free charge carrier yield φ. **d)** Free charge-carrier yield φ multiplied with the sum of free electron and hole mobilities $\Sigma\mu$ in dependence of the laser fluence from TRMC measurements at room temperature of (NOP)$_4$AuB^{III+}I$_8$ with data of three measurements shown for every material.

Charge-Carrier dynamics & Photo conductivity:

In the following, we will discuss charge-carrier dynamics and photo conductivities of the materials, determined with both Time-resolved Microwave Conductivity (TRMC) and Optical-Pump-THz-Probe Spectroscopy (OPTP). The combination of both techniques enables the investigation of charge-carrier dynamics on different time scales from ps (OPTP) to µs (TRMC), leading to a comprehensive picture of the processes involved. Owing to their experimental configuration, for both TRMC and OPTP spectroscopy here, polarization of the probe light lies parallel to the substrate. Therefore, the high degree of crystal orientation of the thin films with *ab*-plane layers parallel to the inorganic octahedral layer means that the obtained signals reflect primarily the in-plane movement of charge-carriers, whereas out-of-plane mobilities along the c-axis cannot be determined.[32,33] OPTP monitors the dynamics of free charge carriers by measuring the fractional change in transmitted THz electric-field amplitude ($-\Delta T/T$) upon pulsed photoexcitation. The OPTP transients measured for thin film samples provide a non-contact measurement of the sheet photoconductivity on ultrafast timescales (see Supporting Information).[34] As shown in **Figure 5a**, OPTP transients measured for NOP-AuAu, NOP-AuBi, and NOP-AuSb thin films reveal a significant decay of the THz photoconductivity within ~1 ps from photoexcitation. Similar ultrafast photoconductivity decays have been reported for various 2D metal halide perovskites,[33,35] including lead and silver-bismuth-based 2D perovskites,[14,36] and have been attributed to either exciton formation or charge-carrier localisation. Owing to the dependence of the observed photoconductivity signal on (i) the electron-hole sum-mobility μ, (ii) the photogenerated charge-carrier density n, and (iii) the photon-to-free-charge branching ratio ϕ, several processes can – in principle – contribute to the observed decay. To further clarify the origin of the observed decay, we performed fluence-dependent OPTP measurements (**Figure S9**). While no clear fluence-dependent dynamics can be observed for NOP-AuBi and NOP-AuSb, the ultrafast THz photoconductivity decay observed for NOP-AuAu is more marked at higher excitation fluence (**Figure 5b**).

On the other hand, for NOP-AuBi and NOP-AuSb, we observe no fluence-dependent dynamics and the remnant photoconductivity after ~1 ps is below the OPTP detection limit ($< 0.05\ \mathrm{cm^2(V\,s)^{-1}}$). Therefore, we speculate that additional processes, such as charge-carrier localization, can contribute to the observed ultrafast decay.[37,38] While we cannot rule out contributions arising from exciton formation in these materials, we note that ultrafast charge-carrier localization has been demonstrated to cause similar fast photoconductivity decays in analogous 2D AgBi-based perovskites and has been linked to the role of reduced electronic dimensionality imposed by the alternating $[AgX_6]^{5-}/[BiX_6]^{3-}$ motif.[39,40] Therefore, we posit that the substitution of Au(III) with Bi(III) and Sb(III) can significantly impact the charge-carrier dynamics and the charge-scattering mechanisms in gold-based 2D perovskites.

To gain further insight into charge-carrier transport in these materials, we estimated the effective electron-hole sum mobility $\mu_{eff} = \phi\mu$ from the THz photoconductivity signal recorded immediately after pulsed photoexcitation.[33,34,39] Importantly, the high time resolution of OPTP measurements gives access to effective mobilities before fast charge-carrier dynamics – such as charge-carrier localization and exciton formation – take place. As reported in Table S4, $(NOP)_4AuAuI_8$ shows a remarkably high effective electron-hole sum mobility of $4.0 \pm 0.2\ \mathrm{cm^2(V\,s)^{-1}}$, similar to that of 2D lead halide perovskites.[33,35] To our knowledge, this is one of the first reports of perovskite-inspired materials showing charge-carrier mobilities capable of competing with their lead-based counterparts. On the other hand, Bi and Sb-based gold perovskites show a significantly reduced charge-carrier mobility, with $0.18 \pm 0.04\ \mathrm{cm^2(V\,s)^{-1}}$ (NOP-AuBi) and $0.19 \pm 0.05\ \mathrm{cm^2(V\,s)^{-1}}$ (NOP-AuSb), which is similar to that reported for 2D-AgBi based perovskites and is compatible with the effects of reduced electronic dimensionality.[14,36,41] Finally, we note that charge-carrier mobilities in 2D perovskites are expected to be highly anisotropic – i.e., high in-plane mobilities within the inorganic layers and low out-of-plane mobilities – as a result of the presence of large organic cations (NOP).[33,42]

To observe charge-carrier population decay over longer timescales, extending up to several microseconds, complementary TRMC measurements were conducted to track free, unbound charge carriers. Photoexcitation was provided by a 2.3 eV laser, with excitation fluences ranging from $1\ \mathrm{\mu J\,cm^{-2}}$ to $60\ \mathrm{\mu J\,cm^{-2}}$. A combination of rapid charge-carrier recombination occurring within the response time of the TRMC setup, along with a potentially high fraction of excitons relative to free charge carriers, only permits an estimation of the lower limit of the total mobility of free charge carriers, yielding $\varphi Sm > 5.5 \cdot 10^{-3}\ \mathrm{cm^2(V\,s)^{-1}}$ for NOP-AuAu, $\varphi Sm > 1.3 \cdot 10^{-3}\ \mathrm{cm^2(V\,s)^{-1}}$ for NOP-AuBi while a free charge carrier mobility greater than $\varphi Sm > 5 \cdot 10^{-5}\ \mathrm{cm^2(V\,s)^{-1}}$ for NOP-AuSb was measurable. The corresponding transient charge-carrier decay for the first two materials (**Figure 5d**) results in charge-carrier lifetimes in the range of multiple μs with a faster initial decay visible for NOP-AuAu compared to NOP-AuBi.

The comprehensive data from OPTP and TRMC indicate a fast generation of free charge-carriers for all three materials to different extents, followed by a rapid cooling to the band edges within the first ps, with fluence-dependent analysis indicating exciton formation for NOP-AuAu. For NOP-AuBi and NOP-AuSb, the absence of fluence-dependent charge-carrier dynamics points towards an ultrafast charge-carrier localization. Subsequently, the system establishes an equilibrium between excitons and free charge carriers, dependent on the exciton binding energy. Both the excitons and the free charge carriers in equilibrium exhibit lifetimes on the order of several microseconds, as evidenced by TRMC measurements.

Electrical conductivity under illumination

Due to their strong absorption in the visible region, their anisotropic structure in combination with the preferred growth direction with the inorganic octahedral layer parallel to the substrate, and their high in-plane conductivity with high charge-carrier mobilities, these materials are anticipated to be interesting candidates for thin-film photodetector materials.

To measure the macroscopic electrical in-plane conductivity and the change of conductivity under illumination, thin films with approx. 400 nm thickness were prepared of the three materials on non-conductive glass substrates coated with Al_2O_3 nanoparticles for enhanced wetting as described in the experimental part. 60-nm thick Ag electrodes were evaporated as top contacts and I/V curves (see Supporting Information) between these contacts in the voltage range of −2 V to 2 V were measured. Since no specific statement can be made about the effective cross-sectional area of the film samples through which the electrical current flows, the measured currents at the maximum applied voltage of −2 V are given instead of calculations of absolute conductivity values.

Table 1: Maximum obtained electrical current at −2 V applied bias under dark conditions and under 1 sun illumination and the light/dark ratio, calculated from the *I*/*V* curve slopes.

	light/dark ratio	I_{max} [μA]
$(NOP)_4AuAuI_8$	2.3	(*l*) 2.98 ± 0.29 (*d*) 1.19 ± 0.21
$(NOP)_4AuBiI_8$	1.0	(*l*) 0.00677 ± 0.0012 (*d*) 0.00669 ± 0.0012
$(NOP)_4AuSbI_8$	1.2	(*l*) 0.0203 ± 0.0024 (*d*) 0.0164 ± 0.0016

(*l*): light; (*d*): dark

Thereby, to our best knowledge an unprecedented high in-plane electrical current for lead-free 2D perovskites was measured, with NOP-AuAu showing the highest in-plane conductivity and 2.3 times increased conductivity under illumination. NOP-AuBi and NOP-AuSb show overall electrical conductivity with obtained electrical currents in the range of nA, which is similar to obtained currents of previously reported Ag-based 2D double perovskites using NOP$^+$ as organic cation. [14] However, NOP-AuBi and NOP-AuSb do not show a significant light/dark ratio. All electrical current values and the light/dark ratios are listed in Table 1. The high electrical conductivity under illumination observed for NOP-AuAu can be explained with its direct band gap in the visible region at 1.48 eV combined with a relatively low exciton-binding energy E_b (Wannier-Mott) calculated at 175 meV and its type II band alignment, which benefits charge carrier dissociation. This demonstrates the potential of gold-based 2-dimensional perovskites as photodetector materials and future potential in solar-cell applications.

Conclusion

In this study, we present the first gold-based Ruddlesden-Popper type 2-dimensional perovskites (NOP)$_4$AuAuI$_8$, (NOP)$_4$AuBiI$_8$, and (NOP)$_4$AuSbI$_8$. All three materials were synthesized from solution *via* spin coating and form homogenous, highly crystalline, [001] direction-oriented thin films with crystallite sizes of hundreds of µm. We showcase their strong optical absorption in the visible region with band gap energies between 1.48 eV (NOP-AuAu) and 2.32 eV (NOP-AuSb), obtained with UV/Vis-spectroscopy. DFT calculations at the HSE06+SOC level of the electronic band structure, transition dipole-moments, and exciton-binding energies confirmed the trend of the experimentally obtained band gap energies and suggested potential for high charge carrier mobilities of the materials. Optical Pump Terahertz Probe spectroscopy combined with Time Resolved Microwave Conductivity revealed unprecedented photoconductivity and effective mobilities for lead-free 2-dimensional perovskite-based materials, as well as charge-carrier lifetimes of multiple µs. Their use as photodetector material was shown through in-plane conductivity measurements under illumination, where a light/dark current ratio of 2.3 was found for NOP-AuAu, highlighting the potential of this material for device applications. This study opens a path towards the design of intriguing future gold-based 2D materials containing different organic cations or through B^{III} cation tuning.

ASSOCIATED CONTENT

Supporting Information. Experimental details, methods, XRD and GIWAXS data, Rietveld refinement details and crystallographic data and CIF files, NMR spectra, thin film morphology micrographs, DFT results, OPTP details and in-plane photoconductivity *IV* curves. This material is available free of charge via the Internet at http://pubs.acs.org.

AUTHOR INFORMATION

Corresponding Author

Thomas Bein– Department of Chemistry and Center for NanoScience (CeNS), University of Munich (LMU), Munich 81377, Germany; orcid.org/0000-0001-7248-5906;
Email: bein@lmu.de

Author Contributions

The manuscript was written through contributions of all authors. All authors have given approval to the final version of the manuscript.

Notes

The authors declare no competing financial interest.

ACKNOWLEDGMENT

We thank Prof. Wolfgang Schnick for support in the evaluation of the crystal data and Laura Spies for the evaluation of the NMR spectrum. Furthermore, the authors thank the Bavarian research network Solar Technologies go Hybrid, the Deutsche Forschungsgemeinschaft (DFG) Excellence Cluster e-conversion (EXC 2089/1 – 390776260) and the DFG focus program SPP 2196 (project DY 18/14-2, No. 424101351) for funding. L.M.H. acknowledges support through a Hans Fischer Senior Fellowship from the Technical University of Munich's Institute for Advanced Study, funded by the German Excellence Strategy. L.M.H. and M.R. acknowledge funding from the UK Engineering and Physical Sciences Research Council (EPSRC). The computations described in this article were performed using the University of Birmingham's BlueBEAR HPC service, the Baskerville Tier 2 HPC service (https://www.baskerville.ac.uk/; funded by the EPSRC and UKRI through the World Class Labs scheme (EP/T022221/1) and the Digital Research Infrastructure program (EP/W032244/1), and the Sulis Tier 2 HPC platform hosted by the Scientific Computing Research Technology Platform at the University of Warwick (funded by EPSRC Grant EP/T022108/1 and the HPC Midlands+ consortium). Through our membership of the UK's HEC Materials Chemistry Consortium, which is funded by the UK Engineering and Physical Sciences Research Council (EPSRC; EP/L000202, EP/R029431, EP/T022213), this computational work also used ARCHER2 UK National Supercomputing Services. D.H., K.B.S. and D.O.S are also grateful to the UK Materials and Molecular Modelling Hub for computational resources, which is partially funded by EPSRC (EP/T022213/1, EP/W032260/1 and EP/P020194/1). D.H. thanks Dr. Christopher N Savory for helpful discussion.

REFERENCES

(1) Mahmud, M. A.; Duong, T.; Peng, J.; Wu, Y.; Shen, H.; Walter, D.; Nguyen, H. T.; Mozaffari, N.; Tabi, G. D.; Catchpole, K. R.; Weber, K. J.; White, T. P. Origin of Efficiency and Stability Enhancement in High-Performing Mixed Dimensional 2D-3D Perovskite Solar Cells: A Review. *Adv. Funct. Mater.* **2022**, *32* (3). DOI: 10.1002/adfm.202009164.

(2) Wang, R.; Mujahid, M.; Duan, Y.; Wang, Z.-K.; Xue, J.; Yang, Y. A Review of Perovskites Solar Cell Stability. *Adv. Funct. Mater.* **2019**, *29* (47). DOI: 10.1002/adfm.201808843.

(3) Sirtl, M. T.; Ebadi, F.; van Gorkom, B. T.; Ganswindt, P.; Janssen, R. A. J.; Bein, T.; Tress, W. The Bottlenecks of Cs 2 AgBiBr 6 Solar Cells: How Contacts and Slow Transients Limit the Performance. *Adv. Opt. Mater.* **2021**, *9* (14). DOI: 10.1002/adom.202100202.

(4) Sirtl, M. T.; Hooijer, R.; Armer, M.; Ebadi, F. G.; Mohammadi, M.; Maheu, C.; Weis, A.; van Gorkom, B. T.; Häringer, S.; Janssen, R. A. J.; Mayer, T.; Dyakonov, V.; Tress, W.; Bein, T. 2D/3D Hybrid Cs 2 AgBiBr 6 Double Perovskite Solar Cells: Improved Energy Level Alignment for Higher Contact-Selectivity and Large Open Circuit Voltage. *Adv. Energy Mater.* **2022**, *12* (7). DOI: 10.1002/aenm.202103215.

(5) Wang, Y.; Liu, J.; Liu, Y.; Li, S.; Xu, X.; Lou, Z. Recent advances in lead-free halide perovskites: from synthesis to applications. *J. Mater. Chem. C* **2024**, *12* (28), 10267–10329. DOI: 10.1039/D4TC01556H.

(6) Savory, C. N.; Walsh, A.; Scanlon, D. O. Can Pb-Free Halide Double Perovskites Support High-Efficiency Solar Cells? *ACS Energy Lett.* **2016**, *1* (5), 949–955. DOI: 10.1021/acsenergylett.6b00471. Published Online: Oct. 12, 2016.

(7) Bhawna; Roy, M.; Vikram; Borkar, H.; Alam, A.; Aslam, M. Spontaneous anion-exchange synthesis of optically active mixed-valence Cs2Au2I6 perovskites from layered CsAuCl4 perovskites. *Chem. comm.* **2021**, 57 (12), 1478–1481. DOI: 10.1039/D0CC06922A.

(8) Wells, H. L. Some complex chlorides containing gold. *Am. J. Sci.* **1922**, *s5-3* (17), 315–326. DOI: 10.2475/ajs.s5-3.17.315.

(9) Kitagawa, H.; Kojima, N.; Takahashi, H.; Mori, N. Electrical conductivity of the perovskite-type mixed-valence compound Cs2Au2I6 under high pressures and low temperature. *Synth. Met.* **1993**, *56* (1), 1726–1729. DOI: 10.1016/0379-6779(93)90314-m.

(10) Kitagawa, H.; Sato, H.; Kojima, N.; Kikegawa, T.; Shimomura, O. Metallization and phase transitions of the three-dimensional halogen-bridge mixed-valence complex Cs2Au2I6 under high pressure. *Solid State Commun.* **1991**, *78* (11), 989–995. DOI: 10.1016/0038-1098(91)90220-p.

(11) Garcia, Y.; Wang, J.; Zhang, T., Eds. *Mössbauer spectroscopy:Applications in chemistry and materials science*; Wiley VCH, 2024. DOI: 10.1002/9783527824953.

(12) Debbichi, L.; Lee, S.; Cho, H.; Rappe, A. M.; Hong, K.-H.; Jang, M. S.; Kim, H. Mixed Valence Perovskite Cs2 Au2 I6 : A Potential Material for Thin-Film Pb-Free Photovoltaic Cells with Ultrahigh Efficiency. *Advanced materials (Deerfield Beach, Fla.)* **2018**, *30* (12), e1707001. DOI: 10.1002/adma.201707001. Published Online: Feb. 6, 2018.

(13) Zhang, P.; Yang, J.-H.; Gong, X.-G. Unusual defect properties in multivalent perovskite Cs2Au2I6 : A first-principles study. *Phys. Rev. Mater.* **2021**, 5 (8). DOI: 10.1103/PhysRevMaterials.5.085405.

(14) Hooijer, R.; Wang, S.; Biewald, A.; Eckel, C.; Righetto, M.; Chen, M.; Xu, Z.; Blätte, D.; Han, D.; Ebert, H.; Herz, L. M.; Weitz, R. T.; Hartschuh, A.; Bein, T. Overcoming Intrinsic Quantum Confinement and Ultrafast Self-Trapping in Ag-Bi-I- and Cu-Bi-I-Based 2D Double Perovskites through Electroactive Cations. *J. Am. Chem. Soc.* **2024**, *146* (39), 26694–26706. DOI: 10.1021/jacs.4c04616. Published Online: Sep. 23, 2024.

(15) Mauck, C. M.; Tisdale, W. A. Excitons in 2D Organic–Inorganic Halide Perovskites. *Trends Chem.* **2019**, *1* (4), 380–393. DOI: 10.1016/j.trechm.2019.04.003.

(16) Passarelli, J. V.; Fairfield, D. J.; Sather, N. A.; Hendricks, M. P.; Sai, H.; Stern, C. L.; Stupp, S. I. Enhanced Out-of-Plane Conductivity and Photovoltaic Performance in n = 1 Layered Perovskites through Organic Cation Design. *J. Am. Chem. Soc.* **2018**, *140* (23), 7313–7323. DOI: 10.1021/jacs.8b03659. Published Online: Jun. 5, 2018.

(17) Fan, Y.; Liu, Q.; Zhang, Z.; Lien, S.-Y.; Xie, Y.; Liang, W.; Gao, P. Gold-Based Double Perovskite-Related Polymorphs: Low Dimensional with an Ultranarrow Bandgap. *Chem. Mater.* **2022**, *34* (4), 1544–1553. DOI: 10.1021/acs.chemmater.1c03195.

(18) Castro-Castro, L. M.; Guloy, A. M. Organic-based layered perovskites of mixed-valent gold(I)/gold(III) iodides. *Angew. Chem., Int. Ed.* **2003**, *42* (24), 2771–2774. DOI: 10.1002/anie.200350929.

(19) Evans, H. A.; Schueller, E. C.; Smock, S. R.; Wu, G.; Seshadri, R.; Wudl, F. Perovskite-related hybrid noble metal iodides: Formamidinium platinum iodide [(FA)2Pt I6] and mixed-valence methylammonium gold iodide [(MA)2Au Au I6]. *Inorg. Chim. Acta* **2017**, *468*, 280–284. DOI: 10.1016/j.ica.2017.04.060.

(20) Murasugi, H.; Kumagai, S.; Iguchi, H.; Yamashita, M.; Takaishi, S. Organic-Inorganic Hybrid Gold Halide Perovskites: Structural Diversity through Cation Size. *Chem. Eur. J.* **2019**, *25* (42), 9885–9891. DOI: 10.1002/chem.201901288. Published Online: Jul. 2, 2019.

(21) Strähle, J.; Gelinek, J.; Kölmel, M.; Nemecek, A.-M. Die Kristallstruktur der Salze K 2 Au 2 I 6 und Cs 2 Ag x Au I1-x Au III Br 6 . Ein Beitrag zur Kristallchemie der Alkalihexahalogenoaurate(I,III) / Crystal Structure of the Salts K 2 Au 2 I 6 and Cs 2 Ag x Au I1-x Au III Br 6 . A Contribution to the Crystal Chemistry of the Alkali Hexahalogeno Aurates(I,III). *Z. Naturforsch. B* **1979**, *34* (8), 1047–1052. DOI: 10.1515/znb-1979-0801.

(22) Matsushita, N.; Tanaka, A.; Kojima, N. A three-dimensional iodo-bridged mixed-valence gold (I, III) compound, Rb2 [AuII2][AuIIII4]. *Acta Crystallogr. Sect. E Struct. Rep. Online* **2005**, *61* (9), i201-i203.

(23) Matsushita, N.; Kitagawa, H.; Kojima, N. A Three-Dimensional Iodo-Bridged Mixed-Valence Gold(I, III) Compound, Cs2AuIAuIIII6.

(24) Shannon, R. D. Revised effective ionic radii and systematic studies of interatomic distances in halides and chalcogenides. *Acta. Cryst. A.* **1976**, *32* (5), 751–767. DOI: 10.1107/S0567739476001551.

(25) Han, D.; Chen, S.; Du, M.-H. Role of Polycyclic Aromatic Alkylammonium Cations in Tuning the Electronic Properties and Band Alignment of Two-Dimensional Hybrid Perovskite Semiconductors. *J. Phys. Chem. Lett.* **2021**, *12* (40), 9754–9760. DOI: 10.1021/acs.jpclett.1c02603. Published Online: Sep. 30, 2021.

(26) Wang, K.; Lin, Z.-Y.; De, A.; Kocoj, C. A.; Shao, W.; Yang, H.; He, Z.; Coffey, A. H.; Fruhling, C. B.; Tang, Y.; Varadharajan, D.; Zhu, C.; Zhao, Y. S.; Boltasseva, A.; Shalaev, V. M.; Guo, P.; Savoie, B. M.; Dou, L. Two-dimensional-lattice-confined single-molecule-like aggregates. *Nature* **2024**, *633* (8030), 567–574. DOI: 10.1038/s41586-024-07925-9. Published Online: Sep. 11, 2024.

(27) Schmitz, A.; Schaberg, L. L.; Sirotinskaya, S.; Pantaler, M.; Lupascu, D. C.; Benson, N.; Bacher, G. Fine Structure of the Optical Absorption Resonance in Cs 2 AgBiBr 6 Double Perovskite Thin Films. *ACS Energy Lett.* **2020**, 5 (2), 559–565. DOI: 10.1021/acsenergylett.9b02781.

(28) Kojima, N.; Kitagawa, H. Optical investigation of the intervalence charge-transfer interactions in the three-dimensional gold mixed-valence compounds Cs2Au2X6(X = Cl, Br or I). *J. Chem. Soc., Dalton Trans.* **1994** (3), 327. DOI: 10.1039/dt9940000327.

(29) Ema, K.; Inomata, M.; Kato, Y.; Kunugita, H.; Era, M. Nearly perfect triplet-triplet energy transfer from Wannier excitons to naphthalene in organic-inorganic hybrid quantum-well materials. *Phys. Rev. Lett.* **2008**, *100* (25), 257401. DOI: 10.1103/PhysRevLett.100.257401. Published Online: Jun. 25, 2008.

(30) Jana, M. K.; Janke, S. M.; Dirkes, D. J.; Dovletgeldi, S.; Liu, C.; Qin, X.; Gundogdu, K.; You, W.; Blum, V.; Mitzi, D. B. Direct-Bandgap 2D Silver-Bismuth Iodide Double Perovskite: The Structure-Directing Influence of an Oligothiophene Spacer Cation. *J. Am. Chem. Soc.* **2019**, *141* (19), 7955–7964. DOI: 10.1021/jacs.9b02909. Published Online: May. 7, 2019.

(31) Chen, X.; Zhou, J.; Xie, Z.; Ma, Y. Excitons in confined molecular aggregates. *Information & Functional Materials* **2024**, *1* (1), 68–86. DOI: 10.1002/ifm2.9.

(32) Dörflinger, P.; Ding, Y.; Schmid, V.; Armer, M.; Turnell-Ritson, R. C.; Ding, B.; Dyson, P. J.; Nazeeruddin, M. K.; Dyakonov, V. Influence of an Organic Salt-Based Stabilizing Additive on Charge Carrier Dynamics in Triple Cation Perovskite Solar Cells. *Adv. Sci.* **2023**, *10* (34), e2304502. DOI: 10.1002/advs.202304502. Published Online: Oct. 9, 2023.

(33) Motti, S. G.; Kober-Czerny, M.; Righetto, M.; Holzhey, P.; Smith, J.; Kraus, H.; Snaith, H. J.; Johnston, M. B.; Herz, L. M. Exciton Formation Dynamics and Band-Like Free Charge-Carrier Transport in 2D Metal Halide Perovskite Semiconductors. *Adv Funct Materials* **2023**, *33* (32). DOI: 10.1002/adfm.202300363.

(34) Wehrenfennig, C.; Eperon, G. E.; Johnston, M. B.; Snaith, H. J.; Herz, L. M. High charge carrier mobilities and lifetimes in organolead trihalide perovskites. *Advanced materials (Deerfield Beach, Fla.)* **2014**, *26* (10), 1584–1589. DOI: 10.1002/adma.201305172.

(35) Kober-Czerny, M.; Motti, S. G.; Holzhey, P.; Wenger, B.; Lim, J.; Herz, L. M.; Snaith, H. J. Excellent Long-Range Charge-Carrier Mobility in 2D Perovskites. *Adv Funct Materials* **2022**, *32* (36). DOI: 10.1002/adfm.202203064.

(36) Hooijer, R.; Weis, A.; Biewald, A.; Sirtl, M. T.; Malburg, J.; Holfeuer, R.; Thamm, S.; Amin, A. A. Y.; Righetto, M.; Hartschuh, A.; Herz, L. M.; Bein, T. Silver-Bismuth Based 2D Double Perovskites (4FPEA) 4 AgBiX 8 (X = Cl, Br, I): Highly Oriented Thin Films with Large Domain Sizes and Ultrafast Charge-Carrier Localization. *Adv. Opt. Mater.* **2022**, *10* (14). DOI: 10.1002/adom.202200354.

(37) Buizza, L. R. V.; Wright, A. D.; Longo, G.; Sansom, H. C.; Xia, C. Q.; Rosseinsky, M. J.; Johnston, M. B.; Snaith, H. J.; Herz, L. M. Charge-Carrier Mobility and Localization in Semiconducting Cu2AgBiI6 for Photovoltaic Applications. *ACS Energy Lett.* **2021**, *6* (5), 1729–1739. DOI: 10.1021/acsenergylett.1c00458. Published Online: Apr. 7, 2021.

(38) Righetto, M.; Caicedo-Dávila, S.; Sirtl, M. T.; Lim, V. J.-Y.; Patel, J. B.; Egger, D. A.; Bein, T.; Herz, L. M. Alloying Effects on Charge-Carrier Transport in Silver-Bismuth Double Perovskites. *J. Phys. Chem. Lett.* **2023**, *14* (46), 10340–10347. DOI: 10.1021/acs.jpclett.3c02750. Published Online: Nov. 10, 2023.

(39) Righetto, M.; Wang, Y.; Elmestekawy, K. A.; Xia, C. Q.; Johnston, M. B.; Konstantatos, G.; Herz, L. M. Cation-Disorder Engineering Promotes Efficient Charge-Carrier Transport in AgBiS2 Nanocrystal Films. *Advanced materials (Deerfield Beach, Fla.)* **2023**, *35* (48), e2305009. DOI: 10.1002/adma.202305009. Published Online: Oct. 24, 2023.

(40) Lal, S.; Righetto, M.; Putland, B. W. J.; Sansom, H. C.; Motti, S. G.; Jin, H.; Johnston, M. B.; Snaith, H. J.; Herz, L. M. The Role of Chemical Composition in Determining the Charge-Carrier Dynamics in (AgI)x(BiI3)y Rudorffites. *Adv Funct Materials* **2024**, *34* (32). DOI: 10.1002/adfm.202315942.

(41) Xiao, Z.; Meng, W.; Wang, J.; Mitzi, D. B.; Yan, Y. Searching for promising new perovskite-based photovoltaic absorbers: the importance of electronic dimensionality. *Mater. Horiz.* **2017**, *4* (2), 206–216. DOI: 10.1039/C6MH00519E.

(42) Righetto, M.; Giovanni, D.; Lim, S. S.; Sum, T. C. The photophysics of Ruddlesden-Popper perovskites: A tale of energy, charges, and spins. *Applied Physics Reviews* **2021**, *8* (1). DOI: 10.1063/5.0031821.

Insert Table of Contents artwork here